POLITECNICO DI TORINO
Repository ISTITUZIONALE

On the turbulent boundary layer over a flat plate at moderate Reynolds numbers

Original
On the turbulent boundary layer over a flat plate at moderate Reynolds numbers / Scarano, F., Jacob, M.C., Carbonneau, X., Gowree, E.R.. - In: PHYSICS OF FLUIDS. - ISSN 1089-7666. - 34:11(2022). [10.1063/5.0124498]

Availability:
This version is available at: 11583/2996655 since: 2025-01-17T08:04:24Z

Publisher:
American Institute of Physics

Published
DOI:10.1063/5.0124498

Terms of use:

This article is made available under terms and conditions as specified in the corresponding bibliographic description in the repository

Publisher copyright
AIP postprint/Author's Accepted Manuscript e postprint versione editoriale/Version of Record

(Article begins on next page)

15 October 2026

Physics of Fluids ARTICLE scitation.org/journal/phf

On the turbulent boundary layer over a flat plate at moderate Reynolds numbers

Cite as: Phys. Fluids **34**, 115150 (2022); doi: 10.1063/5.0124498
Submitted: 6 September 2022 · Accepted: 28 October 2022 ·
Published Online: 18 November 2022

View Online Export Citation CrossMark

Francesco Scarano,[1,a)] Marc C. Jacob,[2] Xavier Carbonneau,[1] and Erwin R. Gowree[1]

AFFILIATIONS

[1]Département Aérodynamique et Propulsion (DAEP) ISAE-SUPAERO, Université de Toulouse, 10, avenue Edouard Belin 31400, Toulouse, France

[2]Laboratoire de Mécanique des Fluides et d'Acoustique, Ecole Centrale de Lyon, France; Institut National des Sciences Appliquées Lyon, France; and Université Claude Bernard Lyon I, Centre National de Recherche Scientifique, Université de Lyon, 36 av. Guy de Collongue, F-69134 Ecully, France

[a)]Author to whom correspondence should be addressed: francesco.scarano@isae-supaero.fr

ABSTRACT

Two separate experimental campaigns of a spatially developing turbulent boundary layer under approximately zero-pressure-gradient at moderate Reynolds numbers ($1700 < Re_\theta < 3400$) are conducted with stereoscopic Particle Image Velocimetry (PIV) and one component Hot Wire Anemometry. This range of Reynolds numbers is found to be of particular interest for turbulent boundary layer control investigations. The motivations behind this work rely on the lack of recent studies that provide a rigorous experimental database on a flat plate turbulent boundary layer, openly available online. This is critical as, in most of the cases, the modification of the statistics resulting from turbulent boundary layer control strategies are compared with a smooth baseline reference. The statistics of the velocity fields, obtained with the two techniques, show a good match with the direct numerical simulation in literature results. We focused on the skin friction evaluation by means of Clauser's chart technique. The near wall turbulence activity and the associated coherent structures are investigated by means of the Variable Interval Time Averaging technique using the hot wire signal. The influence of the acquisition and algorithm parameters as well as the effect of the Reynolds number are reported. The logarithmic and outer structures are investigated by applying the Uniform Momentum Zones technique to the PIV dataset. The hierarchical distribution of the uniform momentum zones as a function of the wall distance as well as their variation with the Reynolds number confirm the validity of the attached eddy model even at the moderate Reynolds numbers of the current investigation.

Published under an exclusive license by AIP Publishing. https://doi.org/10.1063/5.0124498

I. INTRODUCTION

Wall bounded turbulent flows are of large interest for different fields. The application goes from aeronautics, where the objective is often to minimize the turbulent skin friction drag (flow control), to heat exchangers and duct flows for fluid/oil supply. Fundamental research activity is ongoing for a complete understanding and modeling of the most important flow features at different Reynolds numbers.

In a turbulent boundary layer, various types of coherent structures manifest themselves. These structures are characterized as recurrent and statistically relevant patterns that explain the complex flow physics. For the sake of simplicity, these structures can be divided into different types depending on their location in the turbulent boundary layer. The coherent structures that are located in the viscosity dominated near wall region, where most of the turbulent kinetic energy is produced, contribute to the near wall cycle, whereas those of the logarithmic region and the outer region are associated with the energy containing motion and to the bulk production (Marusic and Monty, 2019).

This distinction is less rigorous for low Reynolds numbers where the energy content is so low that the energy containing and viscous scales tend to overlap as evidenced by the reduction of their ratio $\delta/\delta_v = Re_\tau$, where δ and δ_v are the outer scale (boundary layer thickness) and the inner scale (viscous length scale), respectively. The latter is given by $\delta_v = U_\tau/\nu$, where U_τ denotes the friction velocity and ν the kinematic viscosity. As a consequence, the logarithmic region tends to vanish or its extension is very small and is sometimes hardly identifiable. The layer between the logarithmic and the viscous regions is the buffer layer and it is where the interaction between the scales is the strongest.

Published under an exclusive license by AIP Publishing

The coherent structures that dominate the production of the turbulent kinetic energy in the near wall region are the streaks (Kline *et al.*, 1967). The streaks are regions of low momentum. They are subjected to oscillations, instability, and lift-up followed by a chaotic breakup in the process called "bursting" (Robinson, 1991). This process, which starts from $Y^+ \cong 30$ and continues with increasing Y^+ (Kline *et al.*, 1967), is responsible for about 70% of the total shear stress and the production of the turbulent kinetic energy in the wall region (Kim *et al.*, 1971). Bursting can be split into ejections and sweeps. An ejection is an instantaneous upward fluid motion characterized by $u < 0$ and $v > 0$ (where u and v are the streamwise and normal-to-wall velocity fluctuations), usually followed by a sweep, which is an instantaneous fluid motion toward the wall characterized by $u > 0$, $v < 0$. The bursting pattern is identifiable by the conditional average of a single component hot wire signal (Rao *et al.*, 1971). Since both events are characterized by $u \cdot v < 0$, these two events, and consequently, the bursting, contribute positively to the Reynolds shear stress $-\rho\overline{uv}$. The Reynolds shear stress influences the mean velocity close to the wall, its near-wall gradient, and consequently, the wall shear stress and the skin friction (Adrian, 2007). The ensemble of processes described above constitutes the near wall cycle that can be considered as independent from the outer flow at sufficiently high Reynolds numbers (Jiménez and Pinelli, 1999).

Attempts of modeling the coherent structures that are statistically relevant in the logarithmic and outer regions can be found in the work by Townsend (1951) and have been extensively reviewed in a recent article by Marusic and Monty (2019). The conceptual model proposed is known as Attached Eddy Model (AEM). According to this model, for sufficiently high Reynolds numbers (sufficient scale separation), the dominant structures in the logarithmic region are large eddies that are attached to the wall and with a range of scales that grows with Re_τ. With general consensus, these eddies are believed to be hairpin-like vortices (Adrian, 2007). These vortices are spatially self-similar, and their geometry as well as their velocity fields scale with the normal-to-wall distance, whereas the energy density is constant. These vortices are organized in "hierarchies," groups of geometrically self-similar eddies at different stages of development. In fact, each vortical structure undergoes a time evolution that leads to geometrical modifications. This means that the individual vortices are not self-similar in time unlike the hierarchies (see Marusic and Monty, 2019). In a wall-bounded flow, the AEM is able to reproduce quite well the properties of the main eddies and the flow statistics, but not the wake region dynamics. Moreover, the properties and the motions of the small scales affected by the viscosity, which are more relevant at low Reynolds numbers and are crucial for near-wall flow control are not recovered by AEM. Nevertheless, the important role of the logarithmic eddies and AEM on skin friction, especially at high Reynolds numbers [and conversely, the decreasing importance of the near wall cycle even at moderate Reynolds numbers, Hwang (2013)], has been recently addressed and must, therefore, be accounted for in turbulent boundary layer control strategies (de Giovanetti *et al.*, 2016).

Ideally, the study of wall turbulence requires data resolved both in space and in time. It is often very challenging to meet both requirements experimentally, especially when conventional facilities and measurement techniques are available. Despite the growing use of numerical simulations, experimentation is still of fundamental interest because it allows one to validate models and test more complex geometries in an environment that is more representative of real-life conditions. In particular, generation of inflow turbulence in simulations over realistic spanwise dimensions still remains a major limitation of unsteady flow computations. Moreover, it remains extremely expensive to obtain long enough time series for proper statistics.

The most common experimental techniques for turbulent boundary layer investigations are Particle Image Velocimetry (PIV) and Hot Wire Anemometry (HWA). The HWA allows one to obtain pointwise measurements (1–3 but usually 1 or 2 velocity components) resolved in time (acquisition frequency up to 100 kHz) while PIV allows one to investigate the two-dimensional (2D) or three-dimensional (3D) (for stereoscopic and tomographic PIV, respectively) flow features that provide a spatial representation of structures not observable with single-point measurements. Despite its rapid progress, time resolved PIV is limited to low frequencies as its accuracy decreases far below the Shannon frequency (Jacob *et al.*, 2016). Hence, HWA is more reliable to study temporal behaviors whereas PIV is ideal for spatial analysis of instantaneous and mean fields.

Even nowadays the majority of turbulent boundary layer experimental investigations are conducted in facilities where only moderate values of Reynolds number (Re_τ) can be achieved. A series of recent papers on the topic of turbulent boundary layer control and skin friction reduction are reported in Table I with their respective Reynolds numbers. These investigations, despite not being fully representative of the flow physics of the current industrial applications (wind turbine blades and long distance oil pipeline $Re_\tau \cong 4000$, B787 at cruise condition $Re_\tau > 6000$), are useful in understanding the modification that the boundary layer undergoes and can give information, which could potentially be extrapolated to higher Reynolds numbers. The turbulent boundary layers achievable on a conventional test facility are usually of moderate thickness $\mathcal{O}(0.01\,\mathrm{m})$. This means that the near wall region can only be surveyed by miniaturized 1C (1 component) hot wire probes and more hardly with miniaturized but larger 2C HWA probes, usually employed for atmospheric wind tunnel measurements. In the majority of cases, even for time resolved PIV, the temporal resolution is not high enough to educe mechanisms having very short time scales. In addition, a conventional PIV setup does not allow measurements in the close proximity of the wall. This means that only the outer scale motion can be resolved reliably.

TABLE I. Some of the experimental research conducted on turbulent boundary layer for flow control in the last five years.

Paper	Re_τ	Re_θ	Technique
Scarano *et al.* (2022)	580–950	1830–3380	HWA
Du *et al.* (2022)	1124	2351	HWA/PIV
Jafari *et al.* (2022)	1044	2397	HWA
Severino *et al.* (2022)	···	3283	HWA
Cafiero and Iuso (2022)	···	2200–4900	HWA/PIV
Li *et al.* (2020)	740	2250	PIV/μ–PIV
Gowree *et al.* (2019)	···	1550–2500	HWA/LDV
Cui *et al.* (2019)	510	···	PIV
Silvestri *et al.* (2018)	···	3771	HWA
Silvestri *et al.* (2017)	···	1927	HWA

Published under an exclusive license by AIP Publishing

TABLE II. Flow and geometrical parameters for the three different test conditions, downstream measurement location.

	U_∞ (m/s)	δ (mm)	Re_θ	Re_τ	U_τ(m/s)	l^+	d^+	ΔX^+	ΔY^+	$Y^+_{\min}$
HW	10	23.2	1753	624	0.44	42	0.14	···	0.35/28	3.3
PIV	10	23.9	1678	658	0.42	···	···	5.78	6.61	48.2
HW	15	23.1	2750	893	0.60	58.0	0.19	···	0.48/38.6	4.5
PIV	15	23.6	2480	922	0.59	···	···	8.19	9.35	66.6
HW	20	22.1	3433	1091	0.78	74.26	0.25	···	0.61/49.5	6.6
PIV	20	22.6	3166	1157	0.78	···	···	10.75	12.3	82.4

Skin friction evaluation is a crucial task for all turbulent boundary layer measurements. Knowing the skin friction means that the friction velocity U_τ is known; this is fundamental as it allows one to correctly compute the inner-scaled statistics. In addition, it is a first way to verify the efficiency of potential flow control techniques to be tested. The skin friction evaluation itself on a flat plate boundary layer is not a trivial procedure. A floating element usually requires a complex experimental setup. In addition, due to the low forces involved especially at low Reynolds numbers, very sensitive sensors are required. When only PIV and HWA are available, the skin friction is evaluated from the mean velocity profile applying Clauser's chart technique (Wei *et al.*, 2005).

There are not many recent papers on experimental investigations of a zero pressure gradient turbulent boundary layers developing over flat surfaces where the mean flow, the turbulent structures eduction criteria, as well as the governing and acquisition parameters are provided and summarized. The most recent summary is a comparison between experimental data and DNS results provided by Schlatter *et al.* (2009). The current study investigates the use of conventional HWA and PIV setups to educe information from a turbulent boundary layers of modest thickness at moderate Reynolds numbers, which develops over a flat plate. The aim is to provide an experimental baseline reference for the experimental investigations, especially the ones dedicated to turbulent boundary layer control, at moderate Reynolds numbers.

Two separate experimental campaigns are conducted, three flow conditions are tested, ranging from about $600 < Re_\tau < 1100$ ($1700 < Re_\theta < 3400$). Focus is given on the evaluation of the skin friction by means of Clauser's chart technique using data acquired by both the measurement techniques. The limitations in obtaining some turbulent boundary layer quantities or to perform some analysis with the current setup are underlined. The bursting activity is investigated by the conditional average of the HWA signal using the Variable Interval Time Averaging technique (Blackwelder and Kaplan, 1976). The PIV data are used to detect the Uniform Momentum Zones (UMZs). These pockets of approximately equal streamwise momentum are a manifestation of the hierarchies of self-similar large-scale structures present in the outer region of the boundary layer (Adrian *et al.*, 2000; de Silva *et al.*, 2016).

II. EXPERIMENTAL SETUP

Two separate experimental campaigns (PIV and HWA) are conducted in the closed-loop low Reynolds number wind tunnel of ISAE-SUPAERO. The measured turbulence intensity for the empty tunnel is 0.04% (Chanetz *et al.*, 2020). The length of the test section is 2.5 m in the streamwise direction (X), its width is 1.2 m in the horizontal (spanwise) direction (Z), 0.8 m in the direction normal to the test plate (Y), also referred to as cross-stream direction. The test model is a 2.5 m long, 1.2 m wide flat plate with an elliptic leading edge mounted horizontally in the test section. The experiment has been operated at three velocities, 10, 15, and 20 m/s, that provide three flow conditions. The associated dimensionless boundary layer parameters are summarized in Table II for the two investigation techniques. When the model is mounted into the test section, the turbulent intensity increases to a value of about 0.1%. A 780 μm wire is used to trip the turbulent boundary layer right after the elliptical leading edge. 1.1 m downstream of the leading edge, a 400 mm square plexiglass panel is flush mounted into the plate. The plexiglass allows it to reduce the heat transfer to the wall when the HWA probe is very close to the wall. In addition, the plexiglass is almost transparent to the PIV laser sheet that is shot from the top of the wind tunnel, traverses completely the material allowing a considerable reflection reductions. The investigation region is at the centerline of the plate, 600 mm from both sides of the wind tunnel that is, 25.1–27.2 boundary layer thicknesses δ. As a result, the side effects are negligible and the streamwise developing flow can thus be considered as statistically 2D. A flap at the trailing edge is set at 3.7° during the two experimental campaigns to ensure a close to zero streamwise pressure gradient along the measurement domain. The acceleration parameter is defined as

$$k_a = \frac{\nu}{U_e^2}\frac{dU_e}{dX}, \tag{1}$$

where U_e is the velocity at the edge of the boundary layer and ν is the kinematic viscosity. The acceleration parameter is smaller than 1.6×10^{-6} for all the flow conditions, the values are detailed in Table II. This suggests that the acceleration is not significant, and subsequently, no deviations from the log-law are expected (Patel, 1965).

A sketch of the experimental setup is shown in Fig. 1, and the details of the two investigation techniques are reported hereafter.

A. Hot wire

A Dantec 55P15 boundary layer single hot wire probe is used for the measurements, the values of the diameter d and length l of the wire in wall units are reported in Table II. The operating temperature of the wire is around 230° and the overheat ratio is 1.75.

The hot wire sampling frequency is 20 kHz, the signal is filtered analogically by a DISA 55M01. The motivations and limitations for

Published under an exclusive license by AIP Publishing

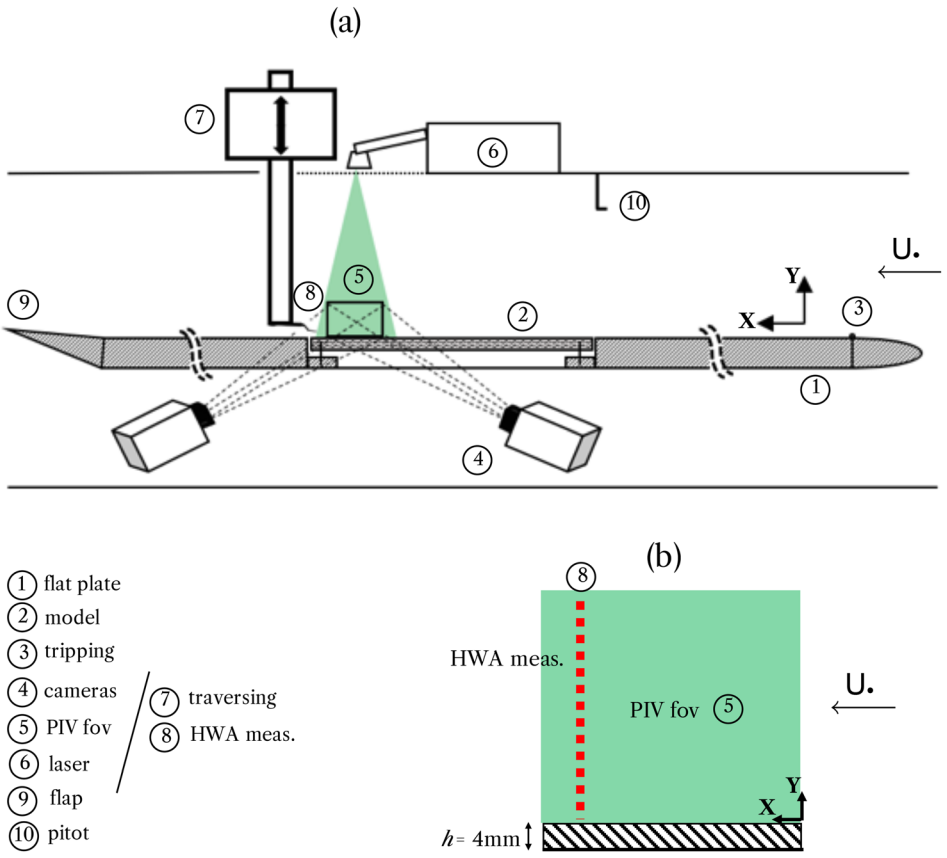

FIG. 1. Sketch of the experimental setup (a) and measurement locations (b). PIV and HWA measurements conducted separately.

this sampling frequency are addressed in Sec. IV. The signal is acquired for over 10 s. The boundary layer turnover is defined as

$$BL_t = \frac{T_t U_\infty}{\delta}, \tag{2}$$

where T_t is the total acquisition time. Mathis *et al.* (2009) suggest that as the wavelength of the largest flow features can exceed 6δ, converged statistics require several thousands of boundary layer turnovers. The values in the current investigation are between 5000 and 10 000 depending on the flow condition, below the value of 15 000 prescribed by Mathis *et al.* (2009) but high enough to obtain the mean and standard deviation converged within 2% and the skewness converged within 5%. King's law was applied to convert voltage into velocity and the hot wire was calibrated *in situ* against a pitot probe.

The hot wire probe was connected to a probe holder. The stiffness of the probe-holder and the NACA0012 shaped probe support allowed to minimize possible vibrations during the acquisition process. The probe support was fixed to a three axes traversing system with minimum displacement of 12.5 μm (between 0.35 and 0.61 viscous lengths). In the current experiment, only one displacement axis in the normal-to-plate direction (Y) is active. Streamwise and spanwise positions were fixed during each traverse (automated by a LabVEW command). The near-wall alignment (performed manually) is guaranteed by the optical probe-to-wall alignment proposed by Gowree *et al.* (2015). A Nikon D5100 equipped with a 300 mm lens and a Kenko Teleconverter 2× are used. The probe-wall distance is estimated with an accuracy of 9 μm (between 0.23 and 0.44 viscous lengths).

The error associated with the hot wire measurement is evaluated following the method proposed by Jørgensen (2002). The error in the velocity sample is 3.13% with 95% confidence interval; the error associated with the momentum thickness is 3.55% while the error in the skin friction is 3.5%.

B. Particle image velocimetry

A commercial stereoscopic PIV system from Dantec Dynamics is used for the measurements. The measurement plane is parallel to the flow (XY) and the cross-stream directions around a fixed streamwise location. A Litron LDY 304 (527 nm) is used to illuminate the measurement region. The laser is placed on top of the test section and connected to a laser arm, which allows accurately aligning the laser sheet with the targeted measurement region. The laser sheet is shot from the top and across the glass ceiling of the wind tunnel. The maximum energy of the laser is 30 mJ/pulse, which drops down to 20 mJ/pulse when connected to the laser arm. During the experimental campaign, the laser power is set to 65% of the maximum power. The thickness of the laser sheet is approximately 0.5 mm. Black velcro was applied to the surfaces of the tunnel to avoid reflections during the acquisition.

Published under an exclusive license by AIP Publishing

The laser pulse delay Δt is tuned to keep the particle displacement between two images below 10 pixels. For the streamwise planes, the Δt used are 30 μs for 10 m/s, 20 μs for 15 m/s, and 15 μs for 20 m/s.

The flow is seeded with a TOPAS olive oil atomizer located downstream of the diffuser of the tunnel. The seeding particles have an average diameter of 1 μm. For each measurement, the acquisition was started about 15 min after the seeding in order to obtain a sufficiently dense and homogeneous cloud of particles throughout the boundary layer.

The images are taken from the sides through the glass wall by two MIRO LAB 340 cameras with a resolution of 2560 × 1600 pixels per image disposed in a stereoscopic arrangement (stereoscopic angle about 85°). Each camera is equipped with a NIKON 300 mm f/4 lens. DANTEC DynamicStudio 6.4 is used for the calibration, synchronization, laser control, and image acquisition. At each acquisition 1000 statistically independent image pairs are acquired at 50 Hz. With an acquisition time of 20 s, the statistical convergence is acceptable, and the boundary layer turnover is twice the HWA value providing an improvement resolution of the largest flow features.

The samples are processed using 2D3C cross correlation PIV algorithm of DynamicStudio 6.4. The interrogation window size is iteratively reduced passing from 64 × 64 pixel to 32 × 32 with an overlap of 50%. This leads to a grid of 40400 vectors with a field of view (FOV) of 65 × 45 mm^2, which is cropped to 45 × 45 mm^2 ($2\delta \times 2\delta$). The vectors close to the wall have been discarded due to reflections. The minimum value of the $Y^+ = \frac{YU_\tau}{\nu}$ as well as the PIV grid dimensions are reported in Table II.

The uncertainty for the PIV data is calculated using the approach proposed by Sciacchitano and Wieneke (2016) and Sciacchitano (2019). The uncertainty associated with the PIV algorithm is below 0.1 pixels. This leads to an uncertainty in the instantaneous in-plane velocity is below 3.5% and it depends on the normal-to-wall location. The uncertainty in the statistics associated with the random error is below 0.1% for the mean velocity and below 2.0% for the Reynolds Shear stress. The convergence of the mean and the shear stresses is verified and it is further improved by the streamwise averaging.

III. FLOW STATISTICS

The statistics are averaged over time t thus the Reynolds decomposition reads

$$U_i' = U_i + u_i, \tag{3}$$

where U_i' is the instantaneous velocity, U_i (or $\bar{U}_i$) is the time-averaged velocity, and u_i is the fluctuation. In the case of the PIV measurements, keeping the same notation for the Reynolds decomposition, the three mean velocity components in the directions (X, Y, Z) with unit vectors (i, j, k) are (U, V, W).

In the case of the PIV data, the profiles of the statistics and the boundary layer integral quantities presented herein are obtained by averaging the data in the streamwise direction X. This allows better converged mean profiles (Womack *et al.*, 2019) and an easier comparison with the HWA data. The spatial averaging can be considered legitimate despite the streamwise evolution of the inner and outer variables used for to scale the data. To illustrate this statement, the evolution of two scaling variables, δ and U_τ are reported in Fig. 2, where it is also reported the error bar.

The trend (slightly positive for the BL thickness and almost constant for the friction velocity) is in agreement with the streamwise development of the boundary layer. However, as the variation is within the measurement error (the error bar is reported in the figure), the boundary layer can be considered fully developed and in equilibrium.

In Table II, the boundary layer parameters calculated with the two measurement techniques have been summarized. They include the freestream velocity, the boundary layer thickness δ, the integral quantities, such as the momentum thickness θ, the Reynolds number based on the momentum thickness $Re_\theta = (\theta U_\infty)/\nu$ and the friction Reynolds number $Re_\tau = (\delta U_\tau)/\nu$, the spatial resolution, and, for the HW, the length and diameter of the wire in wall units. With the current PIV configuration, the minimum value of Y^+ in the results is between about 50 and 85 depending on the flow conditions. Thanks to the optical monitoring, a value down to $Y^+ \cong 4$ can be reached with HWA measurements. The spatial resolution in wall units is fixed in the PIV case, and it varies for the HWA measurements where a finer discretization in the near wall region is chosen. This yields a finer description of the near wall activity.

The velocity profiles for the three flow conditions are presented from Figs. 3–5. They are scaled using outer variables [freestream velocity and the boundary layer thickness (U_∞, δ)] in Fig. 3 and inner quantities (friction velocity U_τ, viscous length scale $\delta_v = \nu/U_\tau$) in Fig. 4 where the mean velocity profiles in wall units $U^+ = U/U_\tau$ are plotted against the normal to wall position in wall units $Y^+ = Y/\delta_v$.

Another way to scale the mean velocity is to compute the difference between the mean velocity at the outer edge of the boundary layer U_e and the local mean velocity both in wall units. This profile is plotted against the normal-to-wall position non dimensionalized with the

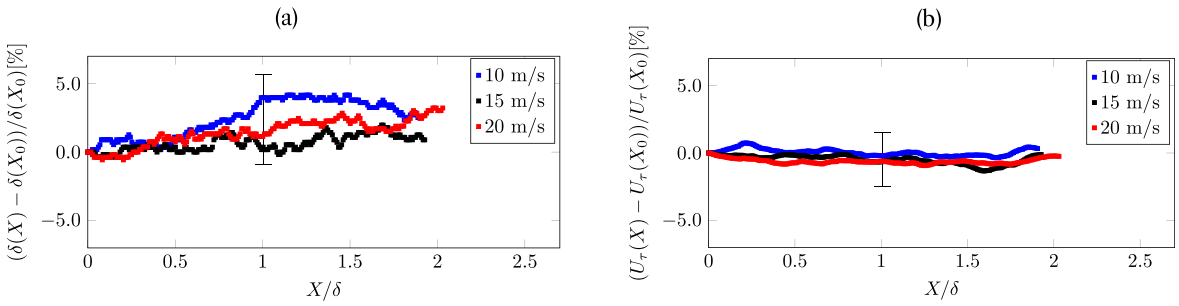

FIG. 2. Streamwise evolution (percentage difference with respect to the leading value) of (a) BL thickness and (b) friction velocity.

Published under an exclusive license by AIP Publishing

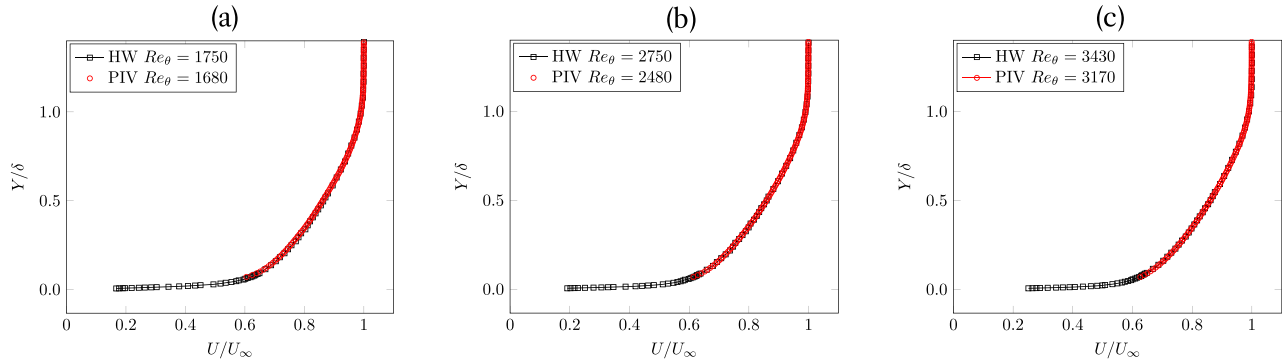

FIG. 3. Mean velocity profile in outer scales, comparison between PIV and HWA data: (a) 10, (b) 15, and (c) 20 m/s (Reynolds number reported in the legend).

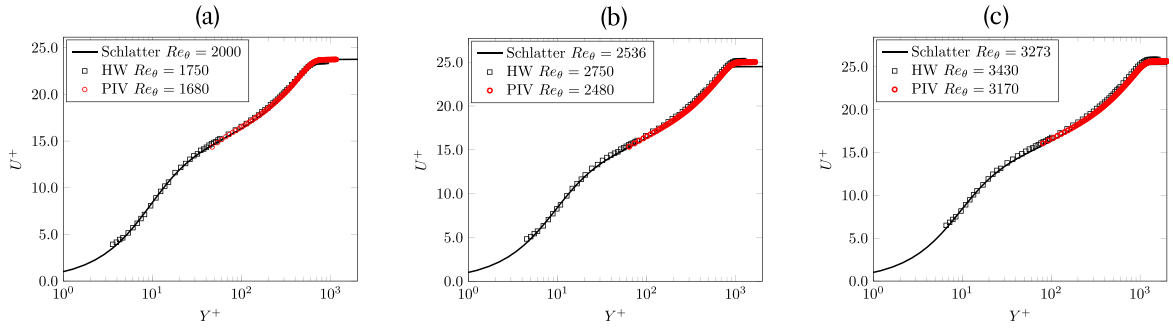

FIG. 4. Mean velocity profile in wall units, comparison between PIV and HWA data and with DNS data by Schlatter and Orlu (2010) (solid line): (a) 10, (b) 15, and (c) 20 m/s (Reynolds number reported in the legend).

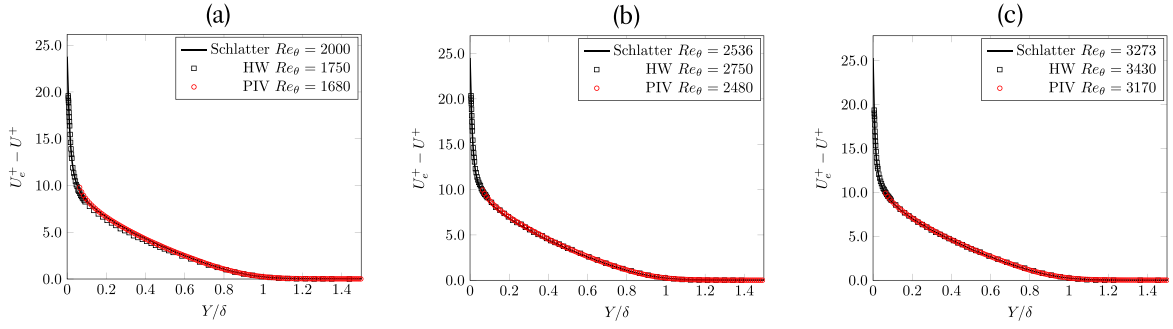

FIG. 5. Velocity defect profile, comparison between PIV and HWA data and DNS data by Schlatter and Orlu (2010) (solid line): (a) 10, (b) 15, and (c) 20 m/s (Reynolds number reported in the legend).

boundary layer thickness Y/δ obtaining the so-called velocity defect profile. In Fig. 5, the velocity defect is plotted for each case showing again a good match between the two datasets and the literature.

The friction velocity U_τ is obtained in both cases by fitting the profiles with the Spalding equation (Kendall and Koochesfahani, 2008; Wei *et al.*, 2005)

$$Y^+ = U^+ + \exp(-kB)\left[\exp(kU^+) - 1 - \frac{(kU^+)^2}{2} - \frac{(kU^+)^3}{6}\right], \quad (4)$$

where k is the von Karman constant and B is the intercept of the universal log law

Published under an exclusive license by AIP Publishing

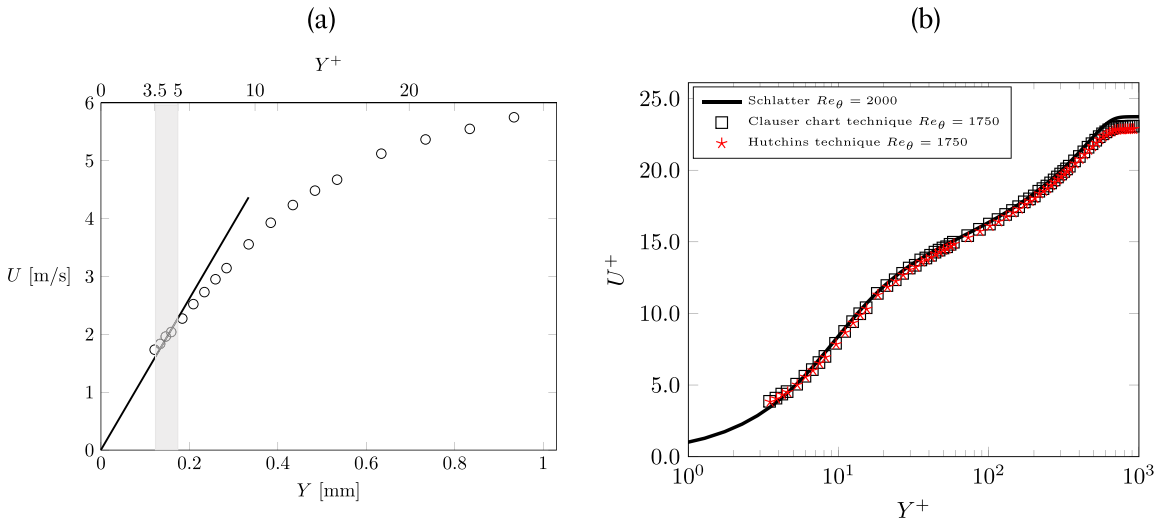

FIG. 6. Mean velocity profile at 10 m/s (a) linear fit of the slope within the linear part of the viscous sublayer, in gray $3.5 < Y^+ < 5$ and (b) comparison of the mean velocity profile in wall units between Clauser chart technique and Hutchins and Choi (2002) method.

$$U^+ = \frac{1}{k}\log(Y^+) + B. \tag{5}$$

For the von Karman constant k, values of $0.39 < k < 0.41$ are most commonly used (George, 2007). According to Zanoun *et al.* (2003) [reported even by Wei *et al.* (2005)], a value $3.5 < B < 6.1$ should be used, and according to George (2007), a value between 4 and 10 is acceptable. In the present case, a value of $k = 0.41$ and $B = 5.5$ are found to fit best.

The Spalding equation is a power-series interpolation that allows one to merge the viscous sublayer region with the logarithmic region. The fit has to be performed over a limited number of points of the velocity profile. The upper limit is dictated by the upper bound of the logarithmic region, which is $Y/\delta \cong 0.15$ independently of the Reynolds number (Marusic and Monty, 2019). In the present experiment, this value is equal to 100, 140, and 180 in wall units for the three flow conditions 10, 15, and 20 m/s, respectively. The aforementioned constraints leads to a different number of points, which have to be fitted to the Spalding equation, in the current case about 30 for the HWA and 10 for the PIV data.

In the paper by Hutchins and Choi (2002), it was stated that an accurate value of U_τ can be obtained by a linear fit of the mean velocity in the viscous sublayer where $U^+ = Y^+$. The region close to the wall $Y^+ < 3.5$ is subjected to heat transfer and confinement effects and should be discarded from the slope computation. Measurements points (at least one) in the region $3.5 < Y^+ < 5$ are necessary. For the current setup, this is found not practical at 15 and 20 m/s (see Table II). At 10 m/s a least squares fit is performed using the three points in $3.5 < Y^+ < 5$ and the extrapolation to zero at the wall. The result reported in Fig. 6 along with Clauser's chart technique results and DNS results by Schlatter and Orlu (2010) shows that the difference in U_τ is found to be less than 1%. The profiles in wall units are almost identical [see Fig. 6(b)] and again confirms the reliability of the Clauser chart technique.

The diagnostic function $Y^+ \cdot \frac{dU^+}{dY^+}$ is presented in Fig. 7 for the three values of Re_θ. The shape of the function shows a good match with the literature. The HWA data show a deviation from the numerical results by Schlatter and Orlu (2010) in the region below $Y^+ \cong 15$. The PIV data overestimate the minimum of the diagnostic function

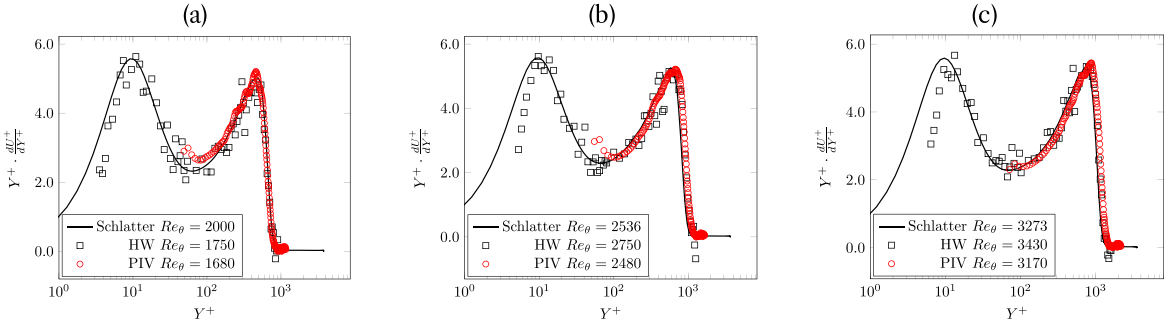

FIG. 7. Diagnostic function, comparison between PIV and HWA data and with DNS data by Schlatter and Orlu (2010) (solid line): (a) 10, (b) 15, and (c) 20 m/s (Reynolds number reported in the legend).

Published under an exclusive license by AIP Publishing

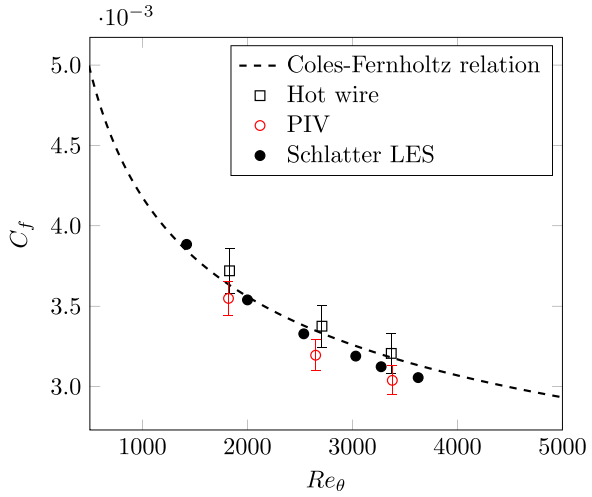

FIG. 8. Friction coefficient obtained using Clauser's chart technique from PIV and HWA results. Coles–Fernholtz relation and results by Schlatter and Orlu (2010) are also reported for comparison.

for at 10 and 15 m/s while for all the flow conditions the match in the outer layer is excellent. The diagnostic function gives an indication of the extension of the logarithmic region by evidencing a plateau of the relative minimum in the overlap region. For the moderate Reynolds number of the current investigation, the asymptotic behavior of the logarithmic region cannot be highlighted. The minima of the diagnostic function for the three flow conditions are in the range $70 < Y^+ 100$. The inverse of the minimum of the diagnostic function gives the von Karman constant k of the universal log law. For the current HWA results, a value of about $k \cong 0.42$ is found.

It has to be underlined here that both the PIV and HWA results match well the numerical results by Schlatter and Orlu (2010) obtained for similar values of the momentum based Reynolds number. Despite the differences explained above, the values of U_τ obtained with PIV and HWA are almost equal. The differences between PIV and HWA are within the uncertainty of the measurements and of the evaluation of the friction velocity and may be due to the fact that the measurements were obtained from two separate experimental campaigns with slightly different values of Re_θ. This comforts the robustness of Clauser's chart technique for estimating the skin friction, even when the measurements points close to the wall are not available as for the PIV dataset.

The skin friction velocity coefficient can be derived from the friction velocity via

$$C_f = 2\left(\frac{U_\tau}{U_\infty}\right)^2. \tag{6}$$

The skin friction drag coefficient is reported in Fig. 8 as a function of the Re_θ and compared with the LES results by Schlatter and Orlu (2010) and the Coles–Fernholz relation for smooth walls

$$C_f = 2[1/k \ln Re_\theta + C]^{-2}, \tag{7}$$

with $k = 0.384$ and $C = 4.127$.

The PIV data provide the vertical component of the velocity field V' and its fluctuation v. This would, in theory, allow the skin friction decomposition following the method proposed by Fukagata *et al.* (2002) or the alternative version by Renard and Deck (2016). Two main limitations of the current PIV dataset have to be underlined. The first limitation is the low spatial resolution, which implies an error in the calculation of the numerical derivatives which is $\mathcal{O}(\Delta X^2, \Delta Y^2)$. However, the method proposed by Senthil *et al.* (2020) slightly reduces this error by removing the streamwise derivative. The second limitation is the lower limit of the field of view $Y^+_{\min}$ that is above 48 for the current dataset. According to Senthil *et al.* (2020), measurements below $Y^+ < 3$ are needed to keep the error in the skin friction evaluation below 10%. For $Y^+_{\min} > 10$, the error is well above 20%. For this reason, a skin friction decomposition is considered inapplicable to the current dataset.

In Fig. 9, the profiles of the streamwise velocity fluctuation root mean square values, σ^+_U, expressed in wall units, are plotted for three different values of Re_θ against Y^+. The current experimental data match well the DNS results of Schlatter and Orlu (2010) in the wake and in the logarithmic region. The peak value of σ^+_U decreases when the Re_θ increases, in opposition to what is observed for the DNS data. According to Örlü and Alfredsson (2010), this different behavior can be attributed to the limited spatial resolution of the hot wire. When the Reynolds number increases, the scale of turbulent eddies is broader and the boundary layer is populated by eddies that have a smaller characteristic size in wall units than the length of the hot wire. In other

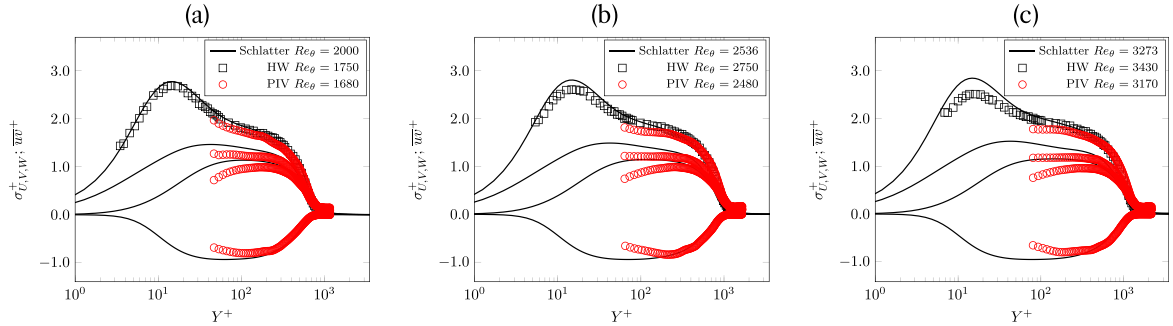

FIG. 9. Shear stresses, comparison between PIV and HWA data and with DNS data by Schlatter and Orlu (2010) (solid line): (a) 10, (b) 15, and (c) 20 m/s (Reynolds number reported in the legend).

Published under an exclusive license by AIP Publishing

words, the hot wire filters out the eddies that are smaller than its spatial resolution which is fixed by the length. For PIV, the filtering is given by the interrogation window size (Sciacchitano and Wieneke, 2016). The values of $\sigma_U^+, \sigma_V^+, \sigma_W^+$ as well as the Reynolds shear stress $\overline{uv}^+$, obtained from PIV data, are reported in Fig. 9. For the shear stress, the near wall peak is not resolved due to the lack of data close to the wall.

All the curves underestimate the reference values of Schlatter and Orlu (2010) near the wall, except for the 10 m/s HWA data that perfectly overlaps the DNS results for σ_U^+. At 15 and 20 m/s, the HWA second-order statistics of the streamwise fluctuations agree much better with the DNS than the PIV. Note that the discrepancies of all statistics increase with the flow velocity. This is in line with the spatial filtering mentioned above: (i) the HWA measurements are better resolved than the PIV; (ii) since the near wall resolution is fixed in geometrical coordinates, it decreases in wall units when the flow speed increases. Additional measurements with longer acquisition time of 30 s were performed to verify the effect of the boundary layer turnover time on the near wall peak. No significant difference between the two measurements was found. This suggests that the acquisition time, at least if the statistics are converged, has negligible effect on the inner peak of σ_U^+.

Despite these differences, the σ_U^+ first peak, which can be seen in the HWA data, lies at $Y^+ \cong 14$, this suggests that the turbulent boundary layer can be considered as a canonical turbulent boundary layers over a flat plate (see Schlatter and Orlu, 2010; Pope, 2000).

The skewness profiles are reported in Fig. 10. The skewness measures the asymmetry in the probability distribution of the velocity signal, and it has been linked by Mathis *et al.* (2009) to the amplitude modulation of the small-scale structures located in the near-wall region by the large-scales structures. At 10 m/s, the skewness is negative in the lower part of the logarithmic region ($0.02 < y/\delta < 0.1$) while in the same range at 15 and 20 m/s, the distribution is almost Gaussian with zero or slightly positive skewness. A similar rise in skewness with Reynolds number has been already reported by Mathis *et al.* (2009). Since the statistical error and the sample duration have found to have only a minor influence on the skewness, the slight discrepancies with the DNS data of Schlatter and Orlu (2010) can be due to the Reynolds numbers differences.

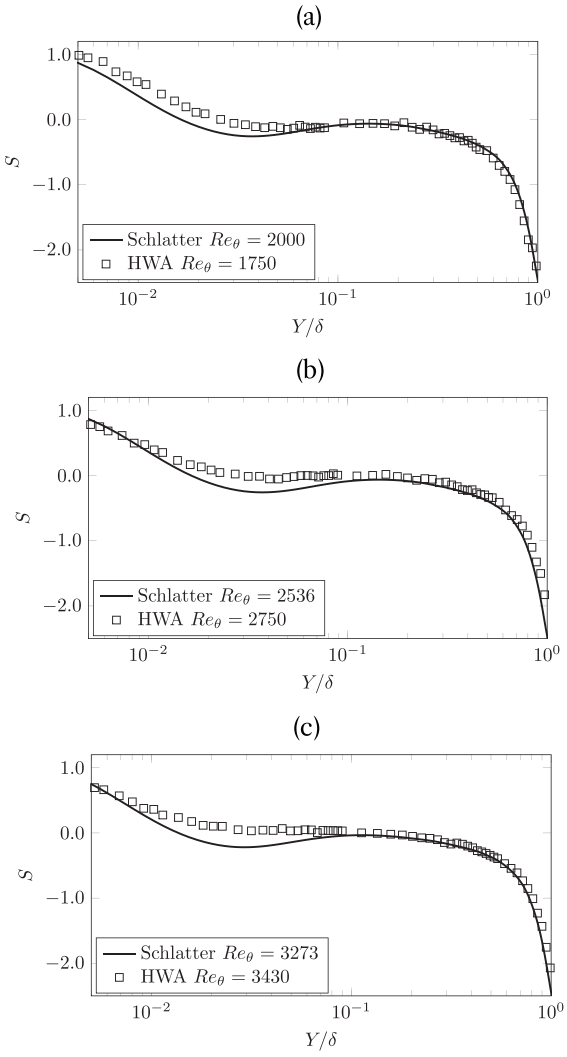

FIG. 10. Skewness profiles, comparison between HWA data and with DNS data by Schlatter and Orlu (2010) (solid line): (a) 10, (b) 15, and (c) 20 m/s (Reynolds number reported in the legend).

IV. NEAR WALL TURBULENT STRUCTURES

A. Turbulent spectra

Frequency spectra are computed from HWA time signal using the Welch algorithm with 98 segments with a window size of 2^{11} samples and no overlap. The energy spectrum describes how turbulent kinetic energy is distributed among the eddies of different sizes (or frequencies as in this case). In Fig. 11, the power spectral density nondimensionalized by the square of the friction velocity (Φ_{UU}/U_τ^2) is plotted together with the $-5/3$ Kolmogorov slope that is representative of the inertial subrange and is valid for high Reynolds numbers. Plot (c) shows that the 20 m/s case can be considered fully turbulent as the inertial subrange is clearly visible. On contrary, for the 15 m/s and more clearly for 10 m/s [plots (b) and (a) respectively], the flow cannot be considered fully turbulent.

The premultiplied spectrum is largely used in turbulence as the integral of the curve represents the turbulent kinetic energy associated with the related component of the velocity. The premultiplied temporal spectra plotted in Fig. 12 against the Strouhal number ($St = f\delta/U_\infty$) are reported at the normal to wall locations $Y^+ = 15$, 30, 100, and 300 (increasing Y^+ in the direction of the arrow) and as 2D contour plots considering all the wall-normal positions. The results agree with the DNS data reported by Schlatter and Orlu (2010) in the sense that the maximum of hump occurs at $St \cong 0.31$ for all the Reynolds numbers tested. The inner region peak at about $Y^+ \cong 15$ can be easily identified. The inner peak intensity at $Y^+ = 15$ decreases with the Reynolds number, once again due to the spatial filtering of the hot wire already discussed. When increasing the Reynolds number, an overall shift of the frequencies toward higher values can be noticed. In addition, the energy associated with higher values of Y^+, corresponding to the outer structures, increases with the Reynolds numbers although the Reynolds numbers are too small to expect an outer peak (Hutchins and Marusic, 2007).

Published under an exclusive license by AIP Publishing

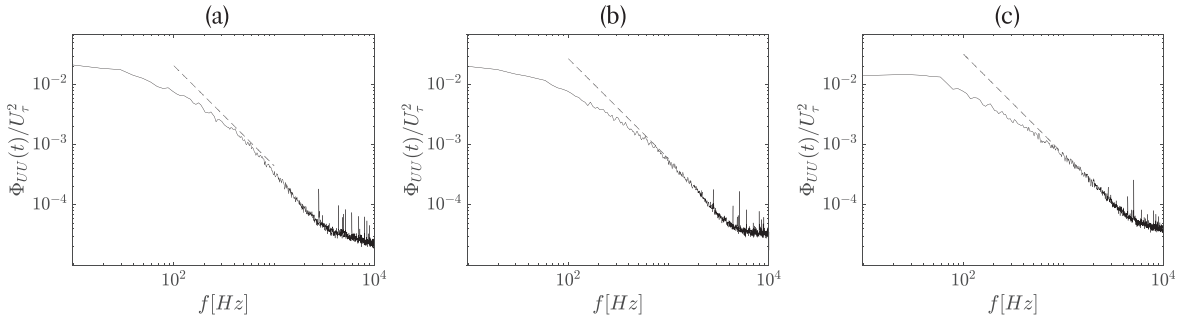

FIG. 11. Spectra of the streamwise velocity fluctuations at $Y^+ = 100$: (a) $Re_\theta = 1750$, (b) $Re_\theta = 2750$, and (c) $Re_\theta = 3430$. Dotted line is $-5/3$ slope.

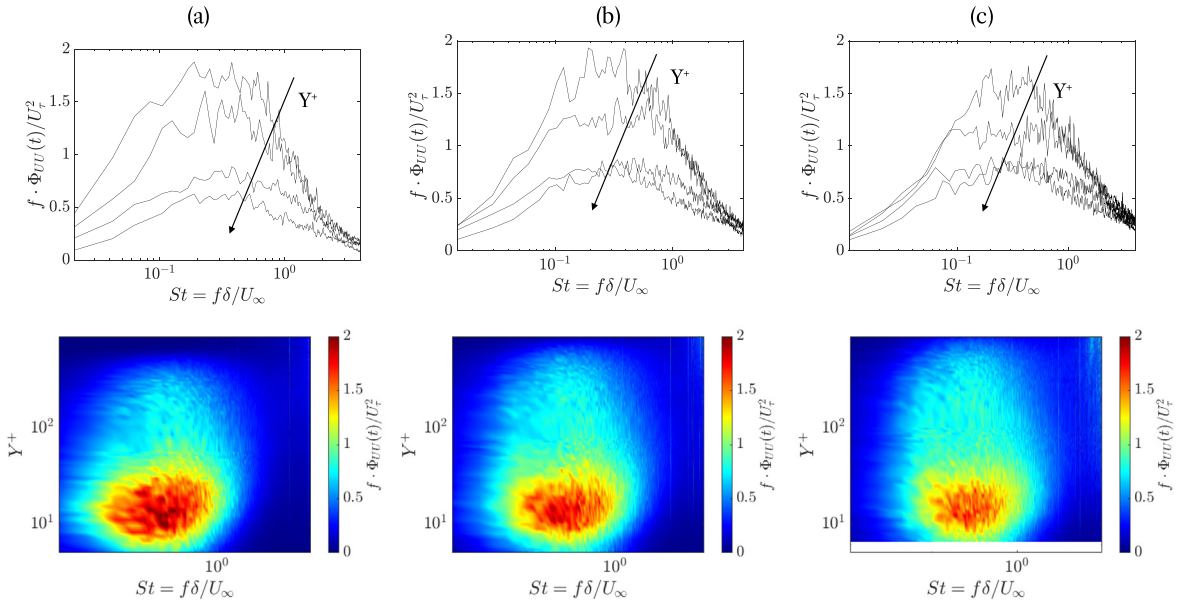

FIG. 12. Premultiplied spectra of the streamwise velocity fluctuations at $Y^+ = 15$, 30, 100, and 300 and 2D contour: (a) $Re_\theta = 1750$, (b) $Re_\theta = 2750$, and (c) $Re_\theta = 3430$. The arrow indicates increasing values of Y^+.

Applying Taylor's hypothesis of frozen turbulence, the streamwise wavelengths λ_X are inferred. The local mean velocity is used as convective velocity. The peaks in the premultiplied spectra correspond to a λ_X^+ of 1700, 1600, and 1350 for 10, 15, and 20 m/s, respectively (not shown here). These values are in good agreement with the streamwise signature of the streaks found by Kline *et al.* (1967).

B. Burst detection

The Variable Interval Time Averaging (VITA) technique was proposed in the seventies by Blackwelder and Kaplan (1976). It is often used to assess the modification of the near wall turbulent activity in the presence of turbulent boundary layer control techniques (Silvestri *et al.*, 2017; Scarano *et al.*, 2022; Severino *et al.*, 2022; Cafiero and Iuso, 2022 to cite the most recent).

In the majority of the studies involving the control of turbulent boundary layer for skin friction drag reduction (as cited in the introduction section), the VITA technique is used and usually compared with the smooth baseline case. We feel that despite this method being developed over a reasonable period just the smooth baseline case is not thoroughly presented. Usually a percentage variation of the intensity or burst frequency with respect to the smooth baseline are reported but without any consideration of the actual values or how they are influenced by the algorithm parameters (k and T^+) or the Reynolds number. In most of the cases, the results are shown only for one or two normal-to-wall locations and this can lead to erroneous assumptions (see Scarano *et al.*, 2022; Silvestri *et al.*, 2017).

The technique is based on the analysis of a single component (1C) hot wire signal, the objective is to detect shear events in the turbulent boundary layer, these events are associated with the bursting activity generated by the passage of one or more coherent structures.

Published under an exclusive license by AIP Publishing

The idea behind the VITA analysis relies on the conditional average of the hot wire signal in a temporal interrogation window which has the characteristic time of the burst. More specifically, a burst is detected when the short-term RMS peak in the interrogation window is larger than long-time RMS of the signal (see Sullivan and Pollard, 1996).

Let $Q'(x_i, t)$ be a quantity varying in space and time. The short term average of the variable over a time interval $2T$ around the current time t is

$$\widehat{Q}(x_i, t, T) = \int_{t-T}^{t+T} Q(x_i, s)ds, \tag{8}$$

from which the temporal local variance can be computed

$$\widehat{\mathrm{var}}(x_i, t, T) = \widehat{U^2}(x_i, t, T) - \left[\widehat{U}(x_i, t, T)\right]^2. \tag{9}$$

The following Heaviside function is used as detection criterion:

$$D(t) = \begin{cases} 1 & \text{if} \quad \widehat{\mathrm{var}}(x_i, t, T) > k \cdot \sigma_U^2, \\ 0 & \text{otherwise}, \end{cases} \tag{10}$$

where σ_U^2 is the variance of the total signal. It is possible to split acceleration events, $\frac{\partial U'}{\partial t} > 0$, representative of the sweeps (Q4) and deceleration events, $\frac{\partial U'}{\partial t} < 0$, representative of the ejections (Q2). This distinction is based only on the streamwise component of the velocity and is less rigorous than quadrant analysis (Wallace, 2016), but it is applicable in the near wall region where the bursting activity is dominant and the quadrant analysis is not applicable with PIV data measured herein.

Two important parameters can be identified, the averaging time T of the short term statistics and the threshold k. A threshold value k between 0.8 and 1.2 is usually employed (Blackwelder and Kaplan, 1976). The time span has to be based on the characteristic time of the duration of a bursting process, namely, between 10 and 20 viscous time scales $T^+ = \frac{TU_\tau^2}{\nu}$ (Blackwelder and Kaplan,1976; Sullivan and Pollard, 1996). If the value of k can be chosen *a posteriori*, the value of T^+ constraints the acquisition frequency. Indeed, a minimal number N_b of samples is required in the time span $2T^+$ to correctly characterize the evolution of a burst. The acquisition frequency is linked to the aforementioned parameters by the formula

$$f_{\mathrm{acqu}} > \frac{N_b U_\tau^2}{2T^+\nu}. \tag{11}$$

This formula permits to set, in the preliminary phases of an experimental campaign, an adequate acquisition frequency knowing only the value of the friction velocity. At least $N_b = 10$ points have found to be necessary to correctly describe a burst, which means that the frequency is strongly influenced by the friction velocity and consequently by the flow Reynolds number as well as by the chosen time span. As the acquisition frequency is linearly dependent on the N_b in order to have a better temporal discretization of the bursts a higher acquisition frequency is needed at higher Reynolds number. In the current experiment, with $f_{\mathrm{acqu}} = 20\,\mathrm{kHz}$, $N_b > 10$ for all the flow conditions and time span described below.

The average burst signature can be obtained by averaging all the detected conditionally sampled events at a given value of Y^+. The burst signature at $Y^+ \cong 20$ is shown in Fig. 13 (for acceleration events) in the three flow conditions, for fixed values of k and T^+. The shape of the burst signature remains unchanged for the three Reynolds numbers associated with 10, 15, and 20 m/s. However, the burst temporal resolution with respect to the burst duration decreases for higher Reynolds numbers and subsequently N_b decreases as well. The "average burst intensity" is defined as the peak-to-peak value of the average burst signature while the "average burst duration" is the temporal interval between two peaks (see Silvestri *et al.*, 2017; Scarano *et al.*, 2022). In the current investigation, an interpolation of the burst signature is performed in order to have a better resolution to compute the average burst duration for the higher Reynolds number.

If the VITA algorithm is applied to all the normal-to-wall acquisition points in the boundary layer, one obtains the "VITA profiles" or "burst profiles": the frequency profile or burst number profile, the burst intensity profile, and the burst duration profile. In Fig. 14, the burst profiles are reported for three values of k and T^+ at 10 m/s in

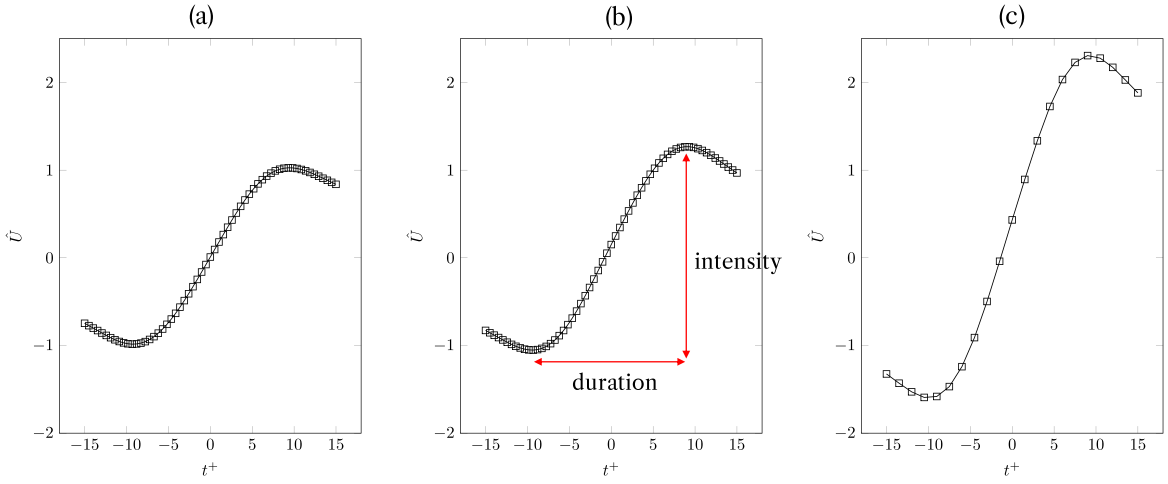

FIG. 13. Average burst signature (acceleration events): (a) $Re_\theta = 1750$, (b) $Re_\theta = 2750$, and (c) $Re_\theta = 3430$. Definition of duration and intensity are reported.

Published under an exclusive license by AIP Publishing

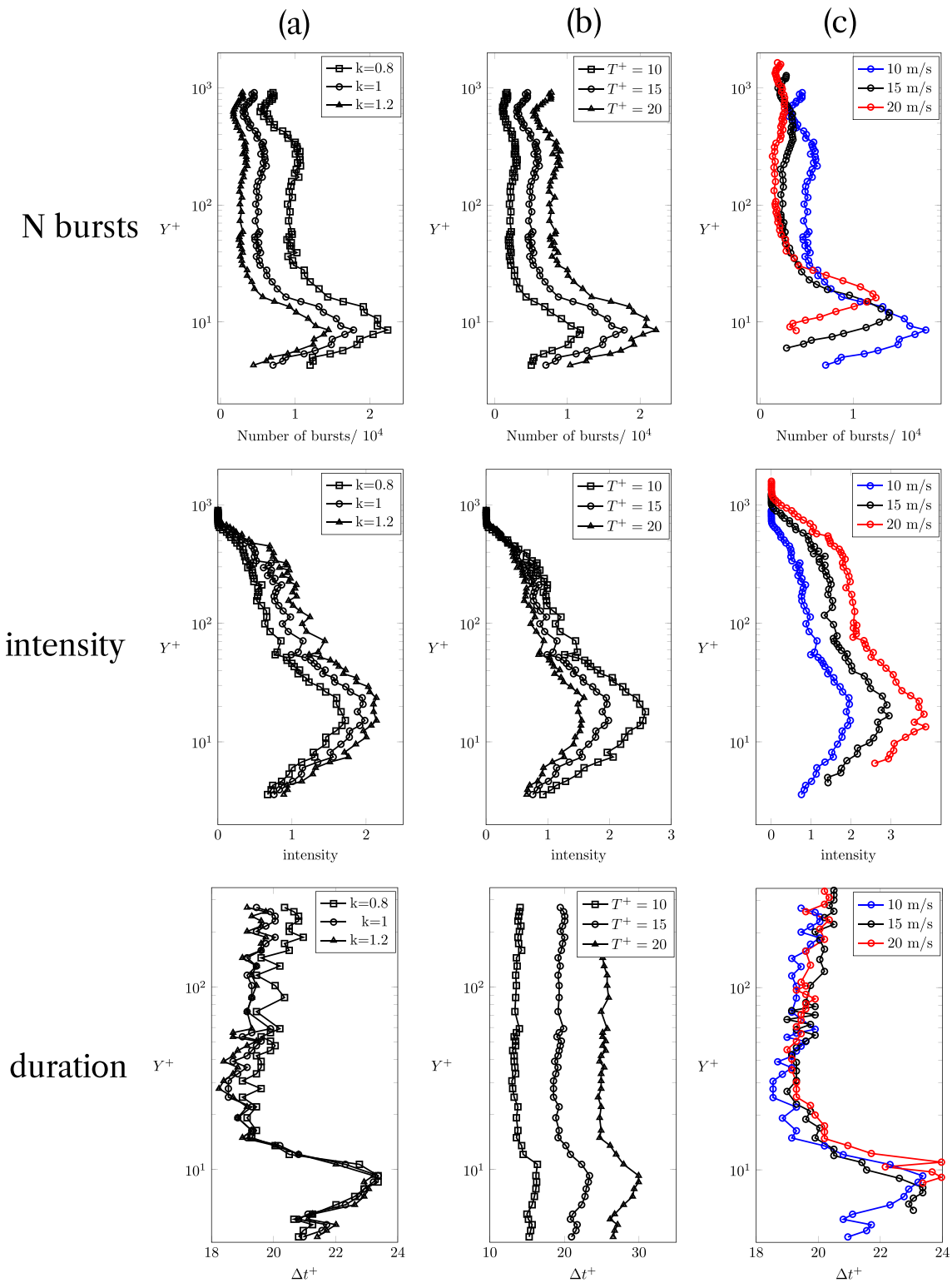

FIG. 14. Burst frequency, intensity, and duration profiles: (a) effect of k for $T^+ = 15$ at $Re_\theta = 1750$ (10 m/s), (b) effect of T^+ for $k = 1$ at $Re_\theta = 1750$ (10 m/s), and (c) effect of the Reynolds number for $k = 1$, $T^+ = 15$.

Published under an exclusive license by AIP Publishing

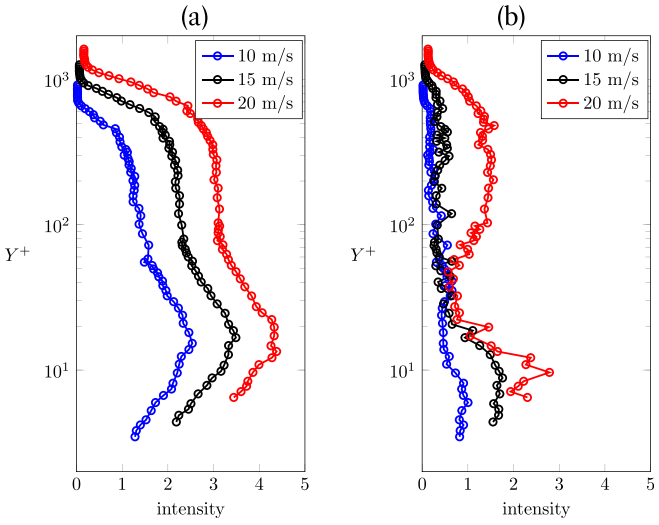

FIG. 15. Intensity profile for the three flow conditions: (a) acceleration events (sweeps, Q2) and (b) deceleration events (ejections, Q4).

(a) and (b), respectively, whereas Fig. 14(c) shows the effect of the Reynolds number for $k = 1$ and $T^+ = 15$. The sampling time is found not to influence the VITA profiles.

The burst frequency profile has a lobe with a peak value between $8 < Y^+ < 16$ depending on the Reynolds number. This is the region of the boundary layer where the bursting activity is dominant as reported by Blackwelder and Kaplan (1976). The outer lobe can be related to the turbulent activity above the logarithmic region, linked to large-scale motions. With increasing Reynolds numbers, both lobes shift upward and attenuate (as discussed hereafter). The peak for the highest Reynolds number is located in the region where most of the turbulent kinetic energy is produced in a canonical boundary layer. It can be further observed that the number of detected bursts decreases as the Reynolds number increases. This is probably due to the decrease in N_b with increasing the Reynolds numbers (at constant acquisition frequency). This prevents from detecting of the bursts with a characteristic time that is too short to be detected. As expected, the effect of increasing k on the burst frequency profiles is to reduce the number of the detection because only the most intense bursts are detected, while the trend is opposite with T^+. Increasing T^+ allows the detection of bursts with longer duration that are filtered out for shorter time spans.

An increase in k corresponds to an increase in the average burst intensity as only the strongest events are detected. The opposite trend is found when increasing T^+, which suggests that the short duration events are stronger than the long duration ones that are filtered out by smaller time spans. The highest intensity peak is located between $10 < Y^+ < 20$ regardless of the Reynolds number. An increase in the peak magnitude can be evinced when Re_θ increases suggesting that the bursts become more intense. The maximum duration of the bursts is around $Y^+ = 10$. The duration profiles appear to depend only weakly on the Reynolds number, while the value of the threshold k has no effect on the profiles. As expected, the duration increases with T^+ as larger events are detected.

The intensity profile obtained by separating the acceleration and deceleration events are reported in Fig. 15. It can be seen that for the higher Reynolds number, there is an increase in the Q2 (ejections) intensity in the outer layer with a clear formation of a second lobe. This suggests that the energy increase in the outer region can be due to an increase in the momentum exchange between the inner and outer regions of the boundary layer. However, in the outer layer, the intensity associated with the deceleration events (ejections) is still lower than that of the acceleration events (sweeps). This partially contradicts the results obtained via quadrant analysis and reported by Wallace (2016). In the outer part of the boundary layer, the Reynolds shear stress due to ejections is predominant. However, it has to be kept in mind that the two techniques are different and that the VITA technique does not take into account the vertical component of the velocity vector.

V. LARGE-SCALE STRUCTURES

A. Uniform momentum zones

The presence of coherent structures in the logarithmic and outer layer can be highlighted by the analysis of a snapshot of the streamwise velocity from a PIV dataset. Zones of approximately equal momentum can be identified (Adrian *et al.*, 2000) (Fig. 16). These zones (called "zones" to be distinguished from the "layers" which are defined with

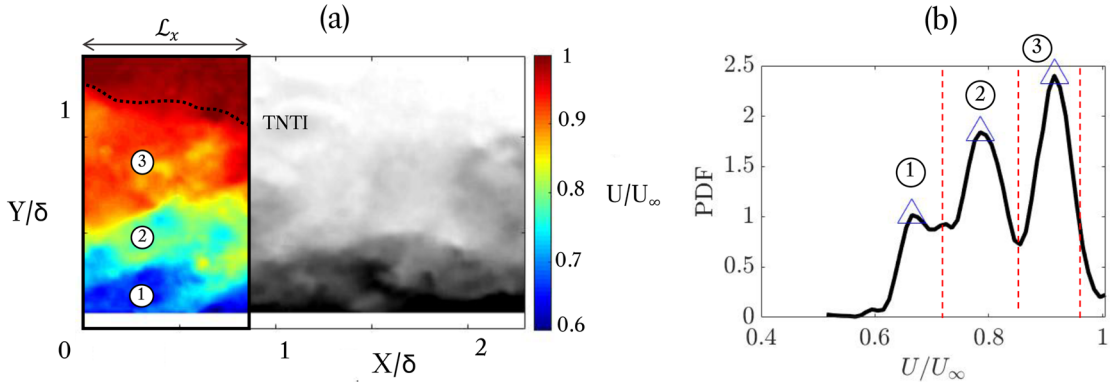

FIG. 16. Uniform momentum zones detection: (a) snapshot and window size $\mathcal{L}_x$ (data inside the colored contour below the TNTI are considered to compute the PDF) and (b) PDF of the streamwise velocity excluding the non-turbulent region, randomly chosen snapshot at 10 m/s, flow from left to right.

Published under an exclusive license by AIP Publishing

respect to the mean flow) are likely to be a manifestation of packets and hierarchies of hairpin vortices which populate the boundary layer. The detection of the so-called Uniform Momentum Zones (UMZs) was first proposed by Meinhart and Adrian (1995) and then further addressed by de Silva *et al.* (2016) and Heisel *et al.* (2020) who strengthened the link between these zonal-like structures and the AEM. They showed that the AEM induces synthetic velocity fields that are compatible with the UMZs identifiable from PIV data. These zones are associated with the most frequent instantaneous velocities in the streamwise velocity field that can be detected from the peaks of the streamwise velocity probability density function (PDF).

A fundamental preliminary step for the correct computation of the PDF consists in the identification of the so-called Turbulent/Non-Turbulent Interface (TNTI) (Chauhan *et al.*, 2014). The detection of the TNTI is fundamental because it allows discarding the vectors outside the turbulent region, which have a value approximately equal to U_∞. The TNTI can be obtained by the turbulent kinetic energy defect, which is calculated considering, for each point of the 2D PIV dataset, a sub-grid of values of 3×3

$$\bar{k}_d = \frac{1}{9U_\infty^2} \sum_{m,n=-1}^{1} \left[(U'_{m,n} - U_\infty)^2 + V'^2_{m,n} \right], \tag{12}$$

where the threshold (in percentage) depends on the turbulent intensity in the wind tunnel (with the test model). In the current investigation this value is set to 0.1%, value which was obtained from HWA measurements (see Sec. II). The TNTI for the current dataset is located in a region within 0.7δ and 1.2δ.

After having discarded the values outside the TNTI, each snapshot is divided in several non-overlapping windows extending each across de the BL over a distance $\mathcal{L}_x$ in the streamwise (see Fig. 16). The PDF of streamwise velocity is then constructed using 60 bins. A correct computation of the PDF requires a sufficient number of velocity vectors; in the current case a value of 15×10^3 vectors is achievable, larger than the value of 5×10^3 reported by de Silva *et al.* (2016). As can be seen from Fig. 16, the relative maxima of the PDF represent the most frequent velocities. These maxima in the streamwise velocity PDF are associated with regions of approximately the modal velocities U_m. The velocity that separates two adjacent zones is named "separation velocity" U_s. According to de Silva *et al.* (2016), it can be computed as the average of two adjacent modal velocity. The separation velocity of the outmost zone and the non-turbulent zone is the velocity of the TNTI interface.

The extension of the spatial window size $\mathcal{L}_x$ has to be the order of one boundary layer thickness (Adrian *et al.*, 2000). At high Reynolds numbers, according to de Silva *et al.* (2016), the influence of $\mathcal{L}_x$ can be neglected in a range of $450 < \mathcal{L}_x^+ < 2500$. A value close to $\mathcal{L}_x^+ \cong 2000$ should be preferred. The parameter $\mathcal{L}_x$ acts as a filter. Increasing the size of $\mathcal{L}_x$, in fact, smooths the PDF thereby reducing the number of UMZ detected (Li *et al.*, 2020). In Fig. 17, the average number of detected number of UMZs is plotted vs $\mathcal{L}_x$. At the moderate Reynolds numbers of the current investigation, and as can be seen even in the study by Li *et al.* (2020), the effect of $\mathcal{L}_x$ cannot be considered as fully negligible. Figure 17 shows that $\mathcal{L}_x > \delta$ should be recommended; in the current investigation the entire FOV has been used to compute the UMZs as done by Cui *et al.* (2019). The resulting window lengths are summarized in Table III, for the three velocities, both in inner and outer scales.

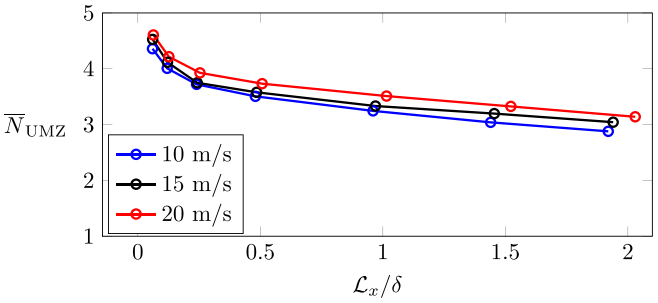

FIG. 17. Effect of the streamwise detection window size $\mathcal{L}_x/\delta$ on the average number of UMZs detected.

TABLE III. Window size chosen based on inner and outer scales.

U_∞ (m/s)	$\mathcal{L}^+$	$\mathcal{L}/\delta$
10	1250	1.92
15	1790	1.94
20	2350	2.03

The PDF of the number of UMZs detected for the three flow conditions is reported in Fig. 18(a). The statistical convergence of the average number of zones detected, $\bar{N}_{UMZ}$, is illustrated in Fig. 18(b). As can be seen from Fig. 19, $\bar{N}_{UMZ}$ systematically increases with the Reynolds number; when plotted against Re_τ the behavior of the mean number of UMZs matches the log-linear relation proposed by de Silva *et al.* (2016). The log-linear increase in the mean number of UMZs is linked to the number of packet-eddy hierarchies in the boundary layer which has itself a log-linear increase with Reynolds number (de Silva *et al.*, 2016; Marusic and Monty, 2019).

It has to be highlighted that the results reported in Fig. 19 strongly suggest that the hierarchical arrangement of the coherent structure in the logarithmic and outer layers can be observed even at moderate Reynolds numbers as those of the current investigation and this is a major finding of the current study. The UMZs are generated by the clustering of low momentum pockets that form beneath one or several hairpin vortices. The thickness of the low momentum regions tends to increase away from the wall. This suggest, in agreement with AEM, the existence of hairpin vortex hierarchies the size of which can be scaled with the normal-to-wall position. The existence of the UMZs at moderate Reynolds numbers would then underlie the presence of hairpin vortices and prove that their hierarchical arrangement is a feature that extends to moderate Reynolds numbers as in the current investigation.

The PDFs of all the modal and separation velocities detected are plotted in Fig. 20. The presence of two peaks in the PDF of the modal velocities and three peaks in the PDF of the separation velocities is brought to light by these plots. Most peaks are slightly more pronounced at higher Reynolds numbers, suggesting that the most frequent modal and separation velocities increasingly dominate the velocity field and the zones become more statistically relevant. Conversely, for the lower Reynolds number, the PDF is slightly smoother for most peaks.

Published under an exclusive license by AIP Publishing

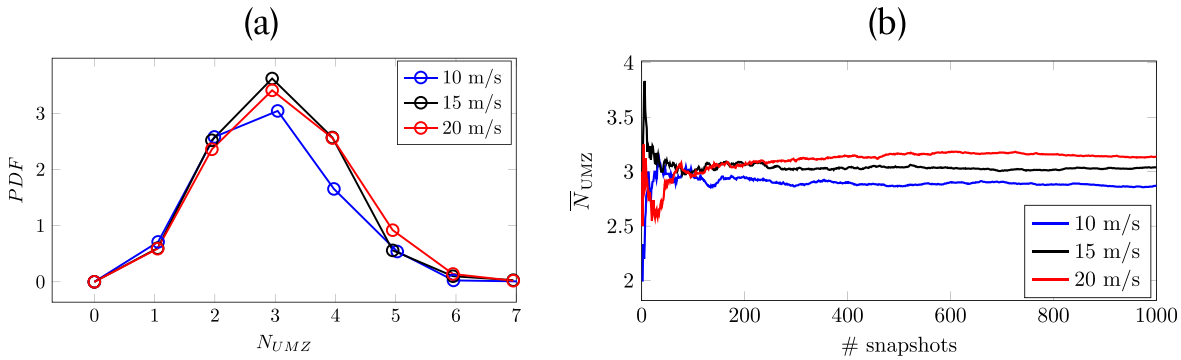

FIG. 18. (a) PDF of the number of UMZs detected and (b) convergence of the mean number of UMZs.

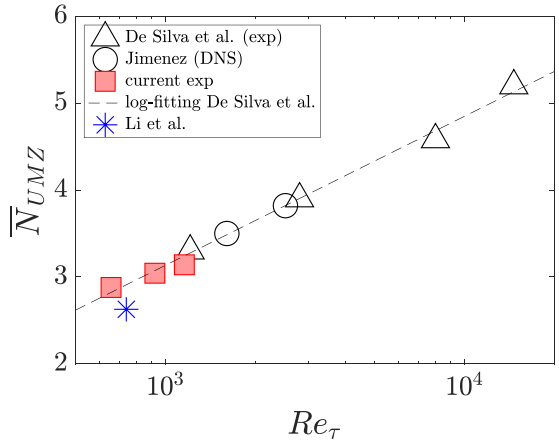

FIG. 19. Log-linear relation between $\bar{N}_{UMZ}$ and Re_τ and literature data.

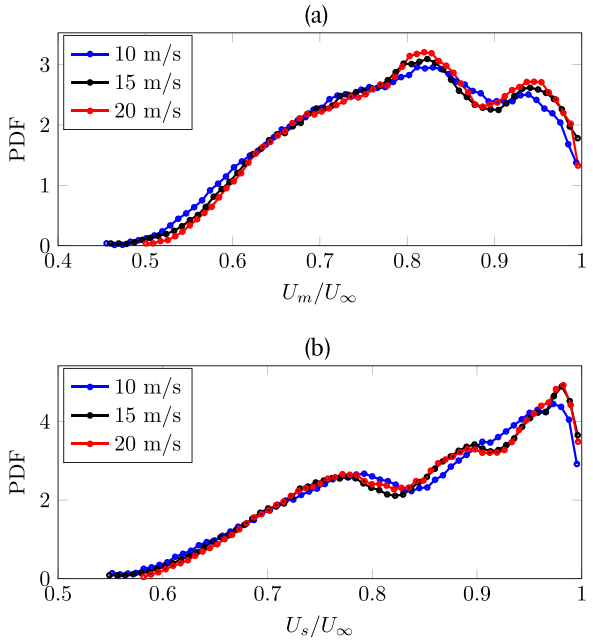

FIG. 20. PDF of the (a) modal and (b) separation velocity for the three flow conditions.

The PDF of the average separation location Y_{sep} and the average "vertical centroid" location Y_{cent} of the detected UMZs are illustrated in Figs. 21 and 22. The average separation location and the centroid are calculated for each snapshot by streamwise averaging the separation locations and the midpoint between two separation locations of two adjacent zones. In both PDFs, two preferential locations for 10 m/s and three for 15 and 20 m/s can be identified. They represent the most frequent separation locations $\tilde{Y}_{sep}/\delta$ and centroid locations $\tilde{Y}_{centr}/\delta$. The outer peak for the separation location represents the most frequent TNTI. The average size t/δ is defined as the streamwise average of the normal-to-wall extension of the zone.

Each zone detected can then be associated with a modal velocity and to an average centroid location. It is possible to compute the PDFs of the modal velocities based on the position of the associated centroid location (Fig. 23). From Fig. 22, three normal-to-wall ranges are chosen $0 < Y_{centr}/\delta < 0.2$, $0.2 < Y_{centr}/\delta < 0.4$, and $0.4 < Y_{centr}/\delta < 0.6$. The effect of the Reynolds number is negligible. In Fig. 23(a) the peaks, representing the most frequent modal velocities, are almost constant for values of U_m/U_∞ approximately equal to 0.65, 0.81, and 0.95.

The change of the average normal-to-wall extent of the structures can be analyzed by looking at the average UMZ normal-to-wall extension t/δ. The average size of the UMZs is reported in Fig. 23(b). The PDFs are computed considered the associated modal velocity momentum deficit $(U_m - U_\infty)/U_\tau$. Three ranges of momentum deficit in wall units are considered: 0–4, 4–8, and 8–12 (increasing momentum deficits correspond to regions that are closer to the wall). Figure 23(b) shows that the average normal-to-wall extent t/δ of the zones increases systematically away from the wall, where the momentum deficit decreases. This result can also be recognized for the single randomly chosen snapshot analyzed in Fig. 21, on this figure, decreasing momentum deficit regions are in the direction of increasing U_m/U_∞. This result is in line with the statement of de Silva *et al.* (2016) who

Published under an exclusive license by AIP Publishing

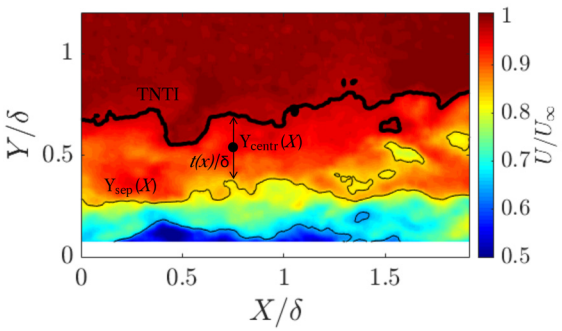

FIG. 21. Randomly chosen snapshot at 10 m/s. Definition of separation location Y_{sep}, centroid location Y_{centr}, and normal-to wall thickness t/δ.

claim that size of the structures scales with the wall distance. Subsequently, the hierarchical length scale distribution of the coherent structures in the BL extends to low Reynolds numbers.

The effect of the Reynolds number seems to be negligible for the two outer zones, while the size of the zone associated with highest momentum deficit significantly grows along with the Reynolds number. Considering that the zone associated with higher momentum deficit approximately corresponds to the logarithmic region of the mean velocity profile, this growth can be related to the increase in the logarithmic layer extension at higher Reynolds numbers.

VI. SUMMARY AND CONCLUSIONS

The majority of recent turbulent boundary layer experiments are conducted at moderate Reynolds numbers due to limitations of the experimental facilities and techniques. The study of the near wall cycle and the bursting activity as well as the modification of the outer structures are necessary steps, especially if the objective is to study the effectiveness of wall bounded turbulence control techniques. The present study aims at providing an experimental dataset of a turbulent boundary layer grazing over a zero pressure gradient flat

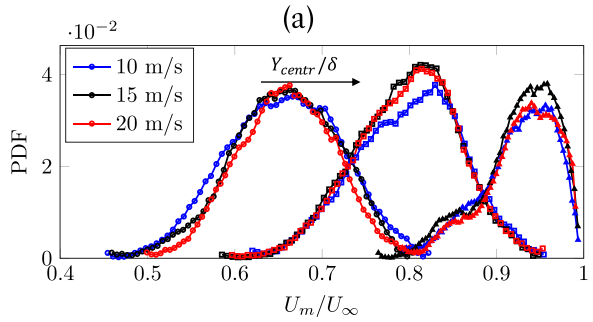

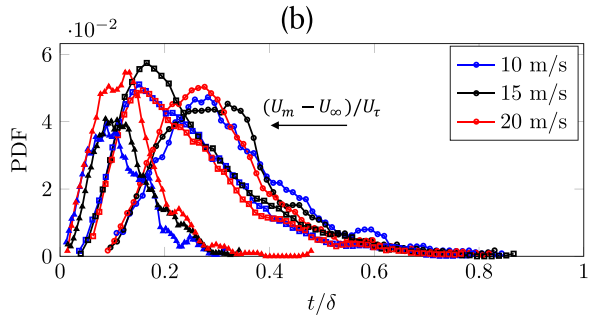

FIG. 23. PDF of (a) the modal velocities grouped with respect to the centroid locations of the zones, 0–0.2, 0.2–0.4, and 0–4–0.6 and (b) extension of the UMZs for the three flow conditions, grouped with respect to momentum deficit ranges 0–4, 4–8, and 8–12.

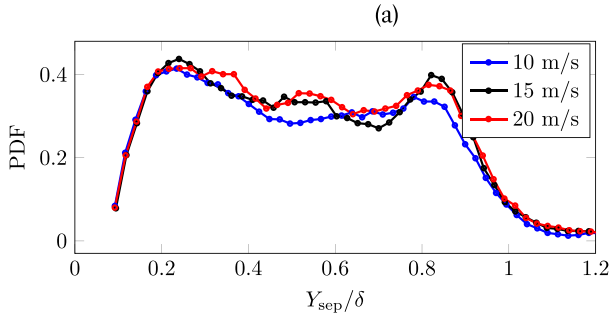

$\tilde{Y}_{sep1}/\delta$	$\tilde{Y}_{sep2}/\delta$	$\tilde{Y}_{sep3}/\delta$
0.23	-	0.80
0.24	0.53	0.82
0.24	0.54	0.81

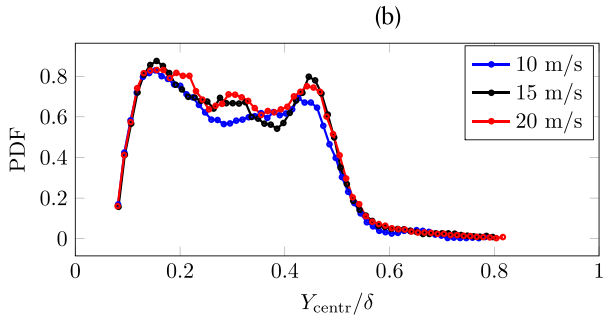

$\tilde{Y}_{cent1}/\delta$	$\tilde{Y}_{cent2}/\delta$	$\tilde{Y}_{cent3}/\delta$
0.15	-	0.44
0.15	0.30	0.46
0.18	0.30	0.46

FIG. 22. PDF of (a) separation location and (b) location of the centroid of the zones.

Published under an exclusive license by AIP Publishing

plate at moderate Reynolds numbers ($1700 < Re_\theta < 3400$, $600 < Re_\tau < 1100$). Two separate experimental campaigns are conducted with a hot wire boundary layer probe connected to a traversing system and a stereoscopic PIV setup.

Statistics are computed from the two experimental datasets. A good match between the two datasets and with DNS data by Schlatter and Orlu (2010) is reached. The evaluation of the skin friction using Clauser's chart technique and the fitting with the Spalding equation is found satisfying showing no significant differences between the two datasets and providing a good match with the literature. The decomposition of the skin friction drag coefficient from the current PIV dataset is not possible due to the lack of measurements close to the wall.

The near wall turbulent cycle is investigated with HWA using the VITA technique. Details about the acquisition parameters as well as the VITA algorithm parameters are provided. The burst profiles (duration, intensity, and frequency) are computed and the variation with the algorithm parameters and the Reynolds number are reported. A peak corresponding to the region where the bursts occur and the turbulent kinetic energy is produced can be highlighted in all VITA profiles.

The near wall region is not captured with the current PIV setup, but the PIV data allow us to compute the Reynolds shear stress. The logarithmic and outer structures are investigated with PIV applying the UMZs technique. The log-linear variation of the average number of uniform momentum zones with Re_τ is correctly captured. The distribution of modal velocities and separation velocities as well as the position of the centroid of the zones and the separation location are reported for the three flow conditions investigated. The size of the zones increases with the normal-to-wall distance as well as the log-linear variation of $\bar{N}_{\mathrm{UMZ}}$ suggests that the hierarchical distribution of length scales and the attached eddy model are valid even at moderate Reynolds numbers. If the modification of the burst profiles in the presence of skin friction reduction is well documented in the literature, the modification of the UMZs has to be further addressed.

The modification of the number, modal velocity, thickness, and distribution of the centroid location of the uniform momentum zones should reflect a modification in the hairpin vortex hierarchical arrangement which would possibly contribute to the modification of skin friction drag. The UMZs analysis should then allow one to study the modification of the hairpin vortices in the presence of turbulent boundary layer control techniques [some results are reported for spanwise wall oscillations Li *et al.* (2020)] or to study the modification that the boundary layers undergo in the presence of a pressure gradient [a recent work has been published Thavamani *et al.* (2020)] or blowing/suction boundary layers.

ACKNOWLEDGMENTS

The research leading to these results received funding from AID (Agence Innovation Défense) under Grant Agreement No. 2019 65 0028 for the FriDa project. We also thank Rémy Chanton, Henri Dedieu, and Philippe Barricau for technical support during the experimental campaign.

AUTHOR DECLARATIONS

Conflict of Interest

The authors have no conflicts to disclose.

Author Contributions

Francesco Scarano: Conceptualization (lead); Data curation (lead); Investigation (lead); Methodology (lead); Writing – original draft (lead); Writing – review & editing (lead). **Marc C Jacob:** Conceptualization (equal); Funding acquisition (lead); Project administration (equal); Supervision (equal); Writing – review & editing (equal). **Xavier Carbonneau:** Supervision (equal). **Erwin Ricky Gowree:** Conceptualization (equal); Funding acquisition (equal); Investigation (equal); Supervision (equal); Writing – review & editing (equal).

DATA AVAILABILITY

The data that support the findings of this study are available from the corresponding author upon reasonable request.

REFERENCES

Adrian, R. J., "Hairpin vortex organization in wall turbulence," Phys. Fluids **19**(4), 041301 (2007).
Adrian, R. J., Meinhart, C. D., and Tomkins, C. D., "Vortex organization in the outer region of the turbulent boundary layer," J. Fluid Mech. **422**, 1–54 (2000).
Blackwelder, R. F. and Kaplan, R. E., "On the wall structure of the turbulent boundary layer," J. Fluid Mech. **76**(1), 89–112 (1976).
Cafiero, G. and Iuso, G., "Drag reduction in a turbulent boundary layer with sinusoidal riblets," Exp. Therm. Fluid Sci. **139**, 110723 (2022).
Chanetz, B., Délery, J., Gilliéron, P., Gnemmi, P., Gowree, E., and Perrier, P., *Experimental Aerodynamics - An Introductory Guide* (Springer Cham, 2020).
Chauhan, K., Philip, J., de Silva, C. M., Hutchins, N., and Marusic, I., "The turbulent/non-turbulent interface and entrainment in a boundary layer," J. Fluid Mech. **742**, 119–151 (2014).
Cui, G., Pan, C., Wu, D., Ye, Q., and Wang, J., "Effect of drag reducing riblet surface on coherent structure in turbulent boundary layer," Chin. J. Aeronaut. **32**(11), 2433–2442 (2019).
de Giovanetti, M., Hwang, Y., and Choi, H., "Skin-friction generation by attached eddies in turbulent channel flow," J. Fluid Mech. **808**, 511–538 (2016).
de Silva, C. M., Hutchins, N., and Marusic, I., "Uniform momentum zones in turbulent boundary layers," J. Fluid Mech. **786**, 309–331 (2016).
Du, H., Li, Q., Zhang, Q., Zhang, W., and Yang, L., "Experimental study on drag reduction of the turbulent boundary layer via porous media under nonzero pressure gradient," Phys. Fluids **34**(2), 025110 (2022).
Fukagata, K., Iwamoto, K., and Kasagi, N., "Contribution of Reynolds stress distribution to the skin friction in wall-bounded flows," Phys. Fluids **14**(11), L73–L76 (2002).
George, W. K., "Is there a universal log law for turbulent wall-bounded flows?," Philos. Trans. R Soc., A **365**(1852), 789–806 (2007).
Gowree, E., Atkin, C., and Gruppetta, S., "A simple digital-optical system to improve accuracy of hot-wire measurements," Meas. Sci. Technol. **26**, 095303 (2015).
Gowree, E., Jagadeesh, C., and Atkin, C., "Skin friction drag reduction over staggered three dimensional cavities," Aerosp. Sci. Technol. **84**, 520–529 (2019).
Heisel, M., de Silva, C. M., Hutchins, N., Marusic, I., and Guala, M., "On the mixing length eddies and logarithmic mean velocity profile in wall turbulence," J. Fluid Mech. **887**, R1 (2020).
Hutchins, N. and Choi, K.-S., "Accurate measurements of local skin friction coefficient using hot-wire anemometry," Prog. Aerosp. Sci. **38**(4), 421–446 (2002).
Hutchins, N. and Marusic, I., "Large-scale influences in near-wall turbulence," Philos. Trans. R Soc., A **365**(1852), 647–664 (2007).
Hwang, Y., "Near-wall turbulent fluctuations in the absence of wide outer motions," J. Fluid Mech. **723**, 264–288 (2013).
Jacob, M. C., Jondeau, E., and Li, B., "Time-resolved PIV measurements of a tip leakage flow," Int. J. Aeroacoust. **15**(6–7), 662–685 (2016).

Published under an exclusive license by AIP Publishing

Jafari, A., Cazzolato, B., and Arjomandi, M., "Finite-length porous surfaces for control of a turbulent boundary layer," Phys. Fluids **34**(4), 045115 (2022).
Jiménez, J. and Pinelli, A., "The autonomous cycle of near-wall turbulence," J. Fluid Mech. **389**, 335–359 (1999).
Jørgensen, F., *How to measure turbulence with hot-wire anemometers – A practical guide* (Dantec Dynamics, 2001).
Kendall, A. and Koochesfahani, M., "A method for estimating wall friction in turbulent wall-bounded flows," Exp. Fluids **44**, 773–780 (2008).
Kim, H. T., Kline, S. J., and Reynolds, W. C., "The production of turbulence near a smooth wall in a turbulent boundary layer," J. Fluid Mech. **50**(1), 133–160 (1971).
Kline, S. J., Reynolds, W. C., Schraub, F. A., and Runstadler, P. W., "The structure of turbulent boundary layers," J. Fluid Mech. **30**(4), 741–773 (1967).
Li, W., Roggenkamp, D., Paakkari, V., Klaas, M., Soria, J., and Schroder, W., "Analysis of a drag reduced flat plate turbulent boundary layer via uniform momentum zones," Aerosp. Sci. Technol. **96**, 105552 (2020).
Marusic, I. and Monty, J. P., "Attached eddy model of wall turbulence," Annu. Rev. Fluid Mech. **51**(1), 49–74 (2019).
Mathis, R., Hutchins, N., and Marusic, I., "Large-scale amplitude modulation of the small-scale structures in turbulent boundary layers," J. Fluid Mech. **628**, 311–337 (2009).
Meinhart, C. D. and Adrian, R. J., "On the existence of uniform momentum zones in a turbulent boundary layer," Phys. Fluids **7**(4), 694–696 (1995).
Örlü, R. and Alfredsson, P.-H., "On spatial resolution issues related to time-averaged quantities using hot-wire anemometry," Exp. Fluids **49**, 101–110 (2010).
Patel, V. C., "Calibration of the Preston tube and limitations on its use in pressure gradients," J. Fluid Mech. **23**(1), 185–208 (1965).
Pope, S. B., *Turbulent Flows* (Cambridge University Press, 2000).
Rao, K. N., Narasimha, R., and Narayanan, M. A. B., "The 'bursting' phenomenon in a turbulent boundary layer," J. Fluid Mech. **48**(2), 339–352 (1971).
Renard, N. and Deck, S., "A theoretical decomposition of mean skin friction generation into physical phenomena across the boundary layer," J. Fluid Mech. **790**, 339–367 (2016).
Robinson, S. K., "Coherent motions in the turbulent boundary layer," Annu. Rev. Fluid Mech. **23**(1), 601–639 (1991).
Scarano, F., Jacob, M. C., Gojon, R., Carbonneau, X., and Gowree, E. R., "Modification of a turbulent boundary layer by circular cavities," Phys. Fluids **34**(6), 065134 (2022).
Schlatter, P. and Orlu, R., "Assessment of direct numerical simulation data of turbulent boundary layers," J. Fluid Mech. **659**, 116–126 (2010).
Schlatter, P., Örlü, R., Li, Q., Brethouwer, G., Fransson, J. H. M., Johansson, A. V., Alfredsson, P. H., and Henningson, D. S., "Turbulent boundary layers up to re_θ=2500 studied through simulation and experiment," Phys. Fluids **21**(5), 051702 (2009).
Sciacchitano, A., "Uncertainty quantification in particle image velocimetry," Meas. Sci. Technol. **30**, 092001 (2019).
Sciacchitano, A. and Wieneke, B., "Piv uncertainty propagation," Meas. Sci. Technol. **27**, 084006 (2016).
Senthil, S., Kitsios, V., Sekimoto, A., Atkinson, C., and Soria, J., "Analysis of the factors contributing to the skin friction coefficient in adverse pressure gradient turbulent boundary layers and their variation with the pressure gradient," Int. J. Heat Fluid Flow **82**, 108531 (2020).
Severino, G. F., Silvestri, A., Cazzolato, B. S., and Arjomandi, M., "Sensitivity analysis of orifice length of micro-cavity array for the purpose of turbulence attenuation," Exp. Fluids **63**(1), 24 (2022).
Silvestri, A., Ghanadi, F., Arjomandi, M., Cazzolato, B., and Zander, A., "Attenuation of sweep events in a turbulent boundary layer using micro-cavities," Exp. Fluids **58**, 58 (2017).
Silvestri, A., Ghanadi, F., Arjomandi, M., Cazzolato, B., Zander, A., and Chin, R., "Mechanism of sweep event attenuation using micro-cavities in a turbulent boundary layer," Phys. Fluids **30**(5), 055108 (2018).
Sullivan, P. and Pollard, A., "Coherent structure identification from the analysis of hot-wire data," Meas. Sci. Technol. **7**(10), 1498–1516 (1996).
Thavamani, A., Cuvier, C., Willert, C., Foucaut, J., Atkinson, C., and Soria, J., "Characterisation of uniform momentum zones in adverse pressure gradient turbulent boundary layers," Exp. Therm. Fluid Sci. **115**, 110080 (2020).
Townsend, A. A., "The structure of the turbulent boundary layer," Math. Proc. Cambridge Philos. Soc. **47**(2), 375–395 (1951).
Wallace, J. M., "Quadrant analysis in turbulence research: History and evolution," Annu. Rev. Fluid Mech. **48**(1), 131–158 (2016). 122414-034550.
Wei, T., Schmidt, R., and Mcmurtry, P., "Comment on the clauser chart method for determining the friction velocity," Exp. Fluids **38**, 695–699 (2005).
Womack, K. M., Meneveau, C., and Schultz, M. P., "Comprehensive shear stress analysis of turbulent boundary layer profiles," J. Fluid Mech. **879**, 360–389 (2019).
Zanoun, E.-S., Durst, F., and Nagib, H., "Evaluating the law of the wall in two-dimensional fully developed turbulent channel flows," Phys. Fluids **15**(10), 3079–3089 (2003).

Published under an exclusive license by AIP Publishing